

Lattice distortions and octahedral rotations in epitaxially strained LaNiO₃/LaAlO₃ superlattices

M. K. Kinyanjui, Y. Lu, N. Gauquelin, M. Wu, A. Frano, P. Wochner, M. Reehuis, G. Christiani, G. Logvenov, H.-U. Habermeier, G. A. Botton, U. Kaiser, B. Keimer, and E. Benckiser

Citation: *Applied Physics Letters* **104**, 221909 (2014); doi: 10.1063/1.4881557

View online: <http://dx.doi.org/10.1063/1.4881557>

View Table of Contents: <http://scitation.aip.org/content/aip/journal/apl/104/22?ver=pdfcov>

Published by the AIP Publishing

Articles you may be interested in

[Compositional engineering of BaTiO₃/\(Ba,Sr\)TiO₃ ferroelectric superlattices](#)

J. Appl. Phys. **114**, 104102 (2013); 10.1063/1.4820576

[Stoichiometry of LaAlO₃ films grown on SrTiO₃ by pulsed laser deposition](#)

J. Appl. Phys. **114**, 027008 (2013); 10.1063/1.4811821

[Epitaxial growth of \(111\)-oriented LaAlO₃ / LaNiO₃ ultra-thin superlattices](#)

Appl. Phys. Lett. **101**, 261602 (2012); 10.1063/1.4773375

[Correlation between structure and properties in multiferroic La_{0.7}Ca_{0.3}MnO₃/BaTiO₃ superlattices](#)

J. Appl. Phys. **99**, 024105 (2006); 10.1063/1.2161424

[Structural characteristics of epitaxial BaTiO₃ / LaNiO₃ superlattice](#)

J. Appl. Phys. **96**, 584 (2004); 10.1063/1.1759074



Lattice distortions and octahedral rotations in epitaxially strained $\text{LaNiO}_3/\text{LaAlO}_3$ superlattices

M. K. Kinyanjui,^{1,a)} Y. Lu,² N. Gauquelin,^{3,b)} M. Wu,² A. Frano,^{2,4} P. Wochner,² M. Reehuis,⁵ G. Christiani,² G. Logvenov,² H.-U. Habermeier,² G. A. Botton,³ U. Kaiser,¹ B. Keimer,² and E. Benckiser^{2,a)}

¹University of Ulm, Central Facility of Electron Microscopy, Albert-Einstein Allee 11, D-89081, Ulm, Germany

²Max Planck Institute for Solid State Research, Heisenbergstr. 1, D-70569 Stuttgart, Germany

³Canadian Centre for Electron Microscopy, McMaster University, 1280 Main Street West, Hamilton, Ontario L8S 4M1, Canada

⁴Helmholtz-Zentrum Berlin für Materialien und Energie, Wilhelm-Conrad-Röntgen-Campus BESSY II, Albert-Einstein-Str. 15, D-12489 Berlin, Germany

⁵Helmholtz-Zentrum Berlin für Materialien und Energie, Lise-Meitner Campus, Hahn-Meitner-Platz 1, D-14109 Berlin, Germany

(Received 24 March 2014; accepted 22 May 2014; published online 6 June 2014)

Using a complementary combination of x-ray diffraction and atomically resolved imaging we investigated the lattice structure of epitaxial $\text{LaNiO}_3/\text{LaAlO}_3$ superlattices grown on a compressive-strain inducing LaSrAlO_4 (001) substrate. A refinement of the structure obtained from the x-ray data revealed the monoclinic $I 2/c$ 1 1 space group. The $(\text{Ni}/\text{Al})\text{O}_6$ octahedral rotation angle perpendicular to the superlattice plane is enhanced, and the one parallel to the plane is reduced with respect to the corresponding bulk values. High-angle annular dark field imaging was used to determine the lattice parameters within the superlattice unit cell. High-resolution electron microscopy images of the oxygen atoms are consistent with the x-ray results. © 2014 AIP Publishing LLC. [<http://dx.doi.org/10.1063/1.4881557>]

Controlled manipulation of the physical properties of strongly correlated transition-metal oxide (TMO) heterostructures requires an understanding of the individual layer structural properties. Most bulk TMO's with perovskite-type structure, ABO_3 , show distortions described by a combination of tilts and rotations of the BO_6 octahedra and which are important for determining their physical properties. Structural distortions in epitaxially strained TMO thin films have been shown to depend on the structure and strain induced by the substrate.^{1–3} Usually, multilayer and superlattice systems exhibit multiple components with possibly different distortions and several interfaces which makes structural determination difficult. We present a combined X-ray Diffraction (XRD), High Resolution Transmission Electron Microscopy (HRTEM), and High Angle Annular Dark Field (HAADF) study of superlattices composed of correlated metal LaNiO_3 (LNO) and the large band gap insulator LaAlO_3 (LAO). These superlattices have raised particular interest due to the possibility of controlling dimensionality of electronic and magnetic phases for LaNiO_3 layer stack thickness below two pseudocubic unit cells (u.c.).^{4–6}

Effects of epitaxial strain on the local atomic and electronic structure of LaNiO_3 heterostructures were previously investigated using, density functional theory (DFT) calculations,^{7–9} x-ray spectroscopy and diffraction,^{2,10–15} and electron microscopy.^{16–19} In particular, modifications in the NiO_6 octahedra due to epitaxial strain in LaNiO_3 heterostructures are investigated mainly by determining the displacement of

oxygen atoms which is a challenging task.^{3,13,14} Previous work on thin films has shown that these positions can be obtained from the refinement of synchrotron x-ray diffraction data,^{1,3} a difficult task due to the limited number of accessible Bragg reflections. Here, using synchrotron x-ray diffraction and aberration-corrected TEM^{20,21} we show that we can accurately obtain the space group, octahedral rotation pattern and local lattice parameters.

High-quality superlattices with $(4/4) \times 8$ and $(3/3) \times 13$ pseudocubic (pc) unit cells (u.c.) were grown by pulsed laser deposition from stoichiometric LaNiO_3 (LNO) LaAlO_3 targets on compressive-strain inducing LaSrAlO_4 (LSAO) (001) substrates. Both samples show paramagnetic and metallic behavior down to the lowest temperatures.^{4,6} TEM samples were prepared from the $(4/4)$ sample using mechanical polishing followed by Ar^+ -ion milling. HAADF imaging was performed on a FEI Titan 80-300 Cubed[®] TEM equipped with probe and image lense aberration correctors, operated at 200 kV and using a Camera Length of 91 mm (angular range of 62–200 mrad). HRTEM imaging was done using the negative Cs imaging method (NCSI)^{22–24} on a spherical aberration-corrected FEI Titan 80-300 TEM operated at 300 kV. X-ray diffraction (XRD) experiments were carried out at the MPI hard x-ray scattering beamline at the ANKA light source of the Karlsruhe Institute of Technology (KIT), Germany, using 10 keV x-rays to access a large Ewald sphere. A 2D pixel detector (DECTRIS, Pilatus 100 K) was used to collect 91 reflections in total, 20 of which were unique. All measurements were performed at room temperature. Note that within our accuracy we could not observe any structural differences between $(3/3)$ and $(4/4)$ superlattices grown on the same substrate.

^{a)}Authors to whom correspondence should be addressed. Electronic addresses: michael.kinyanjui@uni-ulm.de and benckise@fkf.mpg.de

^{b)}Present address: EMAT, Department of Physics, University of Antwerp, Groenenborgerlaan 171, B-2020 Antwerp, Belgium.

The averaged pc lattice parameters $a_{pc} = b_{pc} = 3.756 \text{ \AA}$, and $c_{pc} = 3.857 \text{ \AA}$ were determined from XRD analysis of the positions of the fundamental reflections with integer hkl . The presence of oxygen octahedral rotations give rise to half-order reflections at $(h/2 \ k/2 \ l/2)$. By evaluating the presence or absence of specific half-order Bragg peaks, we identified the space group (or equivalently the octahedral rotation pattern). We deduced the following reflection conditions: (1) h, k , and l equal n , where n is an odd integer; (2) $h = k \neq l$, $k = l \neq h$, and $l = h \neq k$, corresponding to the Glazer rotation pattern $a^-a^-c^-$ (Ref. 25) with angles $\alpha = \beta = 1.9^\circ$ due to the biaxial strain induced by the substrate ($a = b$) and $\gamma = 11.7^\circ$. The rotation pattern together with the deduced reflection conditions are in agreement with the monoclinic space group $I 2/c 1 1$ (No. 15, standard setting $C 1 2/c 1$), also found in related heterostructures.^{3,13,14} Here, an enlarged unit cell ($a \approx b < c$), with respect to the cubic one, is used with dimensions $\sqrt{2} a_{pc} \times \sqrt{2} a_{pc} \times 2a_{pc}$. The doubled c axis is perpendicular to the superlattice plane (i.e., along the growth direction). Due to the crystal twinning distinction between a and b and the small monoclinic angle α_m (between b and c) cannot be resolved, therefore it is set to 90° for further analysis.

Neglecting extinction generates negligible differences, suggesting that the superlattice is a mosaic of small blocks, in good agreement with rocking curves and atomic force microscopy images indicating a structural coherence length of 300–500 Å.¹⁵ The atomic positions were then refined in space group $I 2/c 1 1$. Since the superlattices are fully strained to the substrates, the fundamental reflections (hkl) with h, k, l being integers in pc notation, overlap with the crystal truncation rod (CTR) of the substrate. The relatively high intensity of the CTR compared to the superlattice reflections makes the integrated intensity of the latter difficult to analyze. Therefore, only half-order reflections were taken into account, since there are no contributions from the tetragonal substrate. The intensity of each reflection was integrated over the entire scanning range followed by subtraction of an almost flat background. The integrated intensities I_{int} were then corrected for the beam footprint and the Lorentz polarization correction in order to obtain the structure factors $|F_{hkl}|^2 = (\sin \eta \sin 2\theta)^{-1} \times I_{\text{int}}$, where $(\sin \eta)^{-1}$ is the beam footprint and $(\sin 2\theta)^{-1}$ the Lorentz polarization correction with θ being the scattering angle. Finally, these factors were refined using the program FullProf.²⁶

The resulting atomic positions and corresponding structure are presented in Table I and Fig. 1, respectively. The Ni-O-Ni bond angles are 174.6° in the out-of-plane and

156.4° in the in-plane direction. The in-plane Ni-O bond lengths are $d_{\text{Ni-O}2} = 1.819(10) \text{ \AA}$ and $2.017(10) \text{ \AA}$, and the out-of-plane one is $d_{\text{Ni-O}1} = 1.931(3) \text{ \AA}$. These results agree qualitatively with work reported previously on LNO thin films³ and $\text{LaNiO}_3/\text{SrMnO}_3$ ^{13,14} superlattices, but differ in details. The out-of-plane Ni-O-Ni angles determined in this work are closer to 180° than the in-plane angles. A similar observation was made based on TEM data on a LaNiO_3 - SrTiO_3 superlattice ($\alpha = 3^\circ, \gamma = 7^\circ$),¹⁹ which were compared to results obtained on LaNiO_3 thin films ($\alpha = 6^\circ - 7^\circ, \gamma = 0^\circ - 1^\circ$),^{3,18} both grown on a tensile-strain inducing substrate. This different behavior of thin films and layers in a superlattice geometry was attributed to the necessity to maintain the oxygen octahedral connectivity at both interfaces in a superlattice.^{1,19}

To map local lattice parameter variations across individual LaNiO_3 and LaAlO_3 layers, we used high-resolution HAADF imaging due to the sensitivity of the method to the chemical composition of individual layers. The image intensity in HAADF is proportional to $\sim Z^n$ ($n \sim 1.7 - 2.0$), where Z is the atomic number.²⁷ Using X-ray diffraction to determine lattice parameters from individual LaNiO_3 and LaAlO_3 layers is difficult due to the limited number of Bragg reflections accessible in the superlattice geometry. Figure 2(a) presents an atomically resolved HAADF image of the LNO-LAO layers in $[0 \ 1 \ 0]_{pc}$ projection. The intensity is dominated by La/Sr atoms ($Z = 57/38$) which appear brightest followed by Ni atoms ($Z = 28$) and Al atoms ($Z = 13$). The LaNiO_3 layer appears brighter due to the difference in the scattering between the Ni and Al atoms in LaNiO_3 and LaAlO_3 layers, respectively ($Z^{\text{Ni}} > Z^{\text{Al}}$).

Figure 2(b) presents the values of the out-of-plane lattice spacing parallel to the growth (001) direction (c_{pc} lattice spacing) and the in-plane lattice spacing parallel to the interface (a_{pc} spacing), which were obtained from the distance between respective La atomic columns. This was done after image background subtraction²⁸ and subsequent fitting of the La atomic column positions with 2D Gaussian function. In Fig. 2(b), the vertical axis shows the lattice parameter value (both a and c) and the horizontal axis shows the layer position along the growth direction. The measured mean distances are $a = 3.74(8) \text{ \AA}$ and $c = 3.86(1) \text{ \AA}$ for the in-plane and

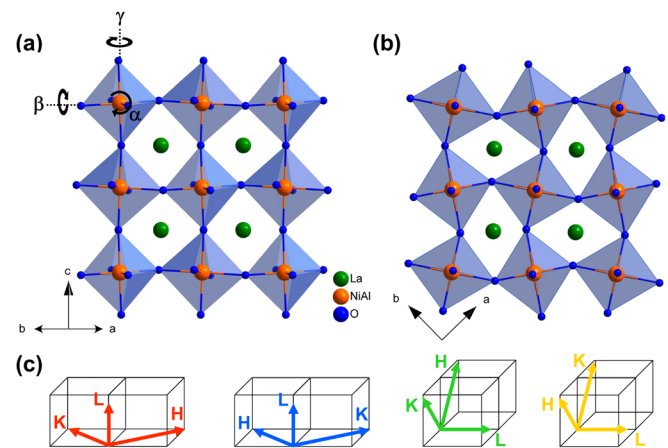


FIG. 1. (a) and (b) Crystal structure of the LNO/LAO superlattice. Compressive strain increases the octahedral rotation $\gamma = 11.6(1)^\circ$ from its value in bulk 5.2° , and reduces $\alpha = \beta$ to $1.9(2)^\circ$. (c) Four out of six possible twin domains occurring in the epitaxial LNO-LAO superlattice.

TABLE I. Atomic positions in the LaNiO_3 - LaAlO_3 superlattice grown on (001) oriented LaSrAlO_4 . The lattice parameter in the monoclinic setting are $a = b = \sqrt{2} a_{pc} = 5.312(2) \text{ \AA}$, $c = 2 c_{pc} = 7.714(5) \text{ \AA}$.

$I 2/c 1 1$	Wyckoff site	x	y	z
La	4e	0.5	0	0.25
Ni	4a	0	0	0
Al	4a	0	0	0
O1	4e	-0.017(3)	0	0.25
O2	8f	0.214(3)	0.313(4)	0.016(1)

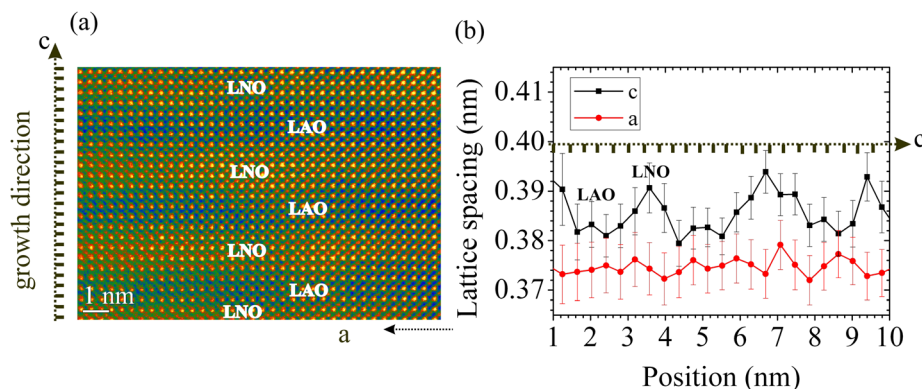


FIG. 2. (a) HAADF image of the $\text{LaNiO}_3/\text{LaAlO}_3$ layers. The LaNiO_3 layers (LNO) show the brightest contrast. The c axis is parallel to the growth direction, while a axis is parallel to the $\text{LaSrAlO}_4\text{-LaNiO}_3$ interface. (b) Distribution of the out-of-plane (c) and in-plane lattice spacing (a). The tick marks on the dotted lines display the position of individual La atomic columns parallel to the growth direction.

out-of-plane distances, respectively, in good agreement with the values determined by XRD (Table I). Note that the lattice parameters obtained from XRD are averaged over a large sample area, and the LNO and LAO layers cannot be distinguished. On the other hand, the lattice parameter obtained using HAADF are highly local and show the variation across the layers and interfaces. The c parameter is larger for the LNO layers compared to the LAO layers, in agreement with the in-plane lattice mismatch of both materials and the LSAO substrate, which is more compressive for LNO. The fact that $a = a_{\text{substrate}} < c$ in a region far from the interface to the substrate indicates that the cation sublattice is fully strained.

In HAADF images, the intensity from the O atomic columns is very weak and therefore possible distortion of the $(\text{Ni}/\text{Al})\text{O}_6$ octahedra cannot be determined. However, the effects of epitaxial strain on the local structure and rotation of the NiO_6 (in LaNiO_3) and AlO_6 (in LaAlO_3) octahedra observed with X-rays are also evident from experimental HRTEM images. Figures 3(a) and 3(b) present HRTEM images obtained from two neighboring layers where the incident electron beam is parallel to the $[100]$ direction. In the

HRTEM images, both the projected structures of the $(\text{Ni}/\text{Al})\text{O}_6$ octahedra and the La atomic columns are well resolved. Since these images were obtained under the NCSI conditions all atomic columns including La, Al, O, and Ni appear as bright dots on a dark background. However, we do observe differences in the intensity and shape of various atom columns in the HRTEM image.

To interpret the HRTEM images, we used calculated HRTEM images based on the bulk LaNiO_3 structure²⁹ and the refined structure (Table I) obtained from X-ray diffraction (Figs. 3(c) and 3(d), respectively). We calculated a series of thickness-defocus HRTEM images and matched these with the experimental image choosing the simulated HRTEM image that best matched the experiments.³⁰ The calculated images are displayed in Figs. 3(c) and 3(d) for LaNiO_3 structure based on refined x-ray data and bulk data, respectively. The calculation parameters for the matching HRTEM image calculations are $C_s = -5 \mu\text{m}$, sample thickness 2 nm, and defocus value = 4 nm. Based on the image simulations, the La and Ni atomic columns are the brightest, while the oxygen atomic columns are less bright. In the simulations based on the structure obtained from the refinement of X-ray diffraction data (Fig. 3(c)), the oxygen atomic columns are blurred and irregular. On the other hand, simulations based on the bulk LaNiO_3 structure (Fig. 3(d)) do not show irregular or blurred oxygen atomic columns. In bulk LaNiO_3 , the tilts of the NiO_6 octahedra are described by the $a^-a^-a^-$ ($\alpha = \beta = \gamma$) tilt system in Glazer's notation.²⁹ Parallel to the $[100]$ direction, the projected HRTEM image of the LaNiO_3 $a^-a^-a^-$ structure shows oxygen columns which are projected symmetrically between two La atoms and on top of the Ni atom (Fig. 3(d)). On the other hand, the refined experimental structures for the LaNiO_3 and LaAlO_3 layers are described by the $a^-a^-c^-$ tilt system ($\alpha = \beta \neq \gamma$). In this case, the projected positions of the oxygen atomic columns parallel to the $[100]$ direction are no longer symmetric as in the $a^-a^-a^-$ bulk case which explains the blurring and the irregular shape of the oxygen atomic columns in the experimental HRTEM images [Figs. 3(a) and 3(b)]. We should point that the effect of blurring and irregular atoms due to the projected image of the $\text{NiO}_6/\text{AlO}_6$ octahedra is best observed in very thin samples. Based on our simulations, this includes sample thickness of up to 4 nm.³⁰ The sample thickness may seem to be quite thin, however a number of papers have already shown experiments and image simulations at sample thicknesses in this range.^{31–34} Indeed, some of us

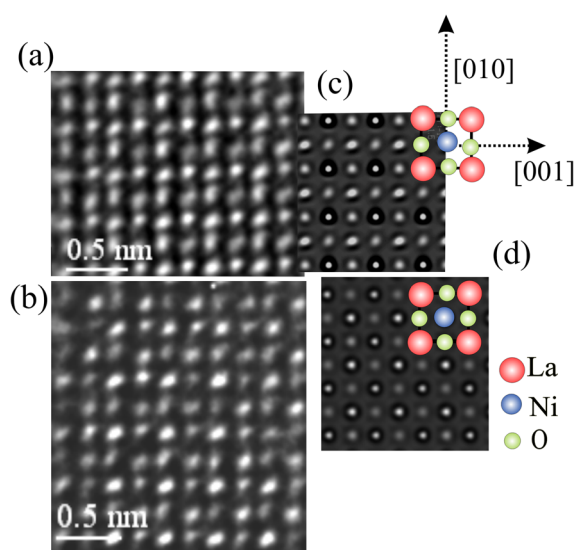


FIG. 3. (a) and (b) Experimental HRTEM images of two neighbouring layers in the $\text{LaNiO}_3/\text{LaAlO}_3$ heterostructure obtained at a small negative C_s value of $< -5 \mu\text{m}$. (c) HRTEM simulation of the LaNiO_3 structure (C_s value = $-5 \mu\text{m}$, sample thickness 2 nm, and defocus value = 4 nm) based on the experimental structure model from the XRD refinements. (d) HRTEM simulation of LaNiO_3 based on the bulk structural model.

have shown that preparation of such thin TEM samples is possible.³⁵ Another issue to take into consideration is sample mistilt and local bending which could also give rise to atomic column blurring. We confirmed that the observed structure of the atomic columns in the experimental HRTEM images is not due to sample mistilt through image simulations incorporating crystal mistilt.³⁰ Since the HRTEM images show a two-dimensional projection of the NiO₆ octahedra, it is difficult to precisely deduce octahedral tilt angles based on the images alone. In TEM, this can be done using position averaged convergent electron beam diffraction.¹⁹ However, HRTEM has the advantage of determining local structural distortions and local defects at much higher spatial resolution. The results of this paper show that the complementary use of X-ray diffraction and high-resolution imaging is a powerful probe of the response of epitaxial TMO multilayers to epitaxial strain.

We are grateful to Sabine Groezinger and Willem van Mierlo for the TEM sample preparation. We gratefully acknowledge financial support by the German Research Foundation (DFG) via TRR80, Project G1 and the Ministry of Science, Research and the Arts (MWK) of the state Baden-Württemberg within the DFG: KA 1295/17-1 Project. We gratefully acknowledge the financial support from NSERC (Discovery Grant) to GAB. The STEM experimental microscopy work was carried out at the Canadian Centre for Electron Microscopy, a National Facility supported by NSERC and McMaster University.

- ¹J. M. Rondinelli, S. J. May, and J. W. Freeland, *MRS Bull.* **37**, 261 (2012).
- ²A. Vaillonis, H. Boschker, W. Siemons, E. P. Houwman, D. H. A. Blank, G. Rijnders, and G. Koster, *Phys. Rev. B* **83**, 064101 (2011).
- ³S. J. May, J.-W. Kim, J. M. Rondinelli, E. Karapetrova, N. A. Spaldin, A. Bhattacharya, and P. J. Ryan, *Phys. Rev. B* **82**, 014110 (2010).
- ⁴A. V. Boris, Y. Matiks, E. Benckiser, A. Frano, P. Popovich, V. Hinkov, P. Wochner, M. Castro-Colin, E. Detemple, V. K. Malik, C. Bernhard, T. Prokscha, A. Suter, Z. Salman, E. Morenzoni, G. Cristiani, H.-U. Habermeier, and B. Keimer, *Science* **332**, 937 (2011).
- ⁵M. Gibert, P. Zubko, R. Scherwitzl, J. Iniguez, and J.-M. Triscone, *Nature Mater.* **11**, 195 (2012).
- ⁶A. Frano, E. Schierle, M. W. Haverkort, Y. Lu, M. Wu, S. Blanco-Canosa, U. Nwankwo, A. V. Boris, P. Wochner, G. Cristiani, H. U. Habermeier, G. Logvenov, V. Hinkov, E. Benckiser, E. Weschke, and B. Keimer, *Phys. Rev. Lett.* **111**, 106804 (2013).
- ⁷P. Hansmann, X. Yang, A. Toschi, G. Khaliullin, O. K. Andersen, and K. Held, *Phys. Rev. Lett.* **103**, 016401 (2009).
- ⁸M. J. Han, C. A. Marianetti, and A. J. Millis, *Phys. Rev. B* **82**, 134408 (2010).

- ⁹A. Blanca-Romero and R. Pentcheva, *Phys. Rev. B* **84**, 195450 (2011).
- ¹⁰J. Chakhalian, J. M. Rondinelli, J. Liu, B. A. Gray, M. Kareev, E. J. Moon, N. Prasai, J. L. Cohn, M. Varela, I. C. Tung, M. J. Bedzyk, S. G. Altendorf, F. Strigari, B. Dabrowski, L. H. Tjeng, P. J. Ryan, and J. W. Freeland, *Phys. Rev. Lett.* **107**, 116805 (2011).
- ¹¹E. Benckiser, M. W. Haverkort, S. Brueck, E. Goering, S. Macke, A. Frano, X. Yang, O. K. Andersen, G. Cristiani, H.-U. Habermeier, A. V. Boris, I. Zegkinoglou, P. Wochner, H.-J. Kim, V. Hinkov, and B. Keimer, *Nature Mater.* **10**, 189 (2011).
- ¹²J. W. Freeland, J. Liu, M. Kareev, B. Gray, J. W. Kim, P. Ryan, R. Pentcheva, and J. Chakhalian, *Europhys. Lett.* **96**, 57004 (2011).
- ¹³S. J. May, C. R. Smith, J.-W. Kim, E. Karapetrova, A. Bhattacharya, and P. J. Ryan, *Phys. Rev. B* **83**, 153411 (2011).
- ¹⁴S. J. May, C. R. Smith, J. W. Kim, E. Karapetrova, A. Bhattacharya, and P. J. Ryan, *Phys. Rev. B* **85**, 039905 (2012).
- ¹⁵M. Wu, E. Benckiser, M. W. Haverkort, A. Frano, Y. Lu, U. Nwankwo, S. Brück, P. Audehm, E. Goering, S. Macke, V. Hinkov, P. Wochner, G. Cristiani, S. Heinze, G. Logvenov, H.-U. Habermeier, and B. Keimer, *Phys. Rev. B* **88**, 125124 (2013).
- ¹⁶E. Detemple, Q. M. Ramasse, W. Sigle, G. Cristiani, H.-U. Habermeier, E. Benckiser, A. V. Boris, A. Frano, P. Wochner, M. Wu, B. Keimer, and P. A. van Aken, *Appl. Phys. Lett.* **99**, 211903 (2011).
- ¹⁷E. Detemple, Q. M. Ramasse, W. Sigle, G. Cristiani, H.-U. Habermeier, B. Keimer, and P. A. van Aken, *J. Appl. Phys.* **112**, 013509 (2012).
- ¹⁸J. Hwang, J. Y. Zhang, J. Son, and S. Stemmer, *Appl. Phys. Lett.* **100**, 191909 (2012).
- ¹⁹J. Hwang, J. Son, J. Y. Zhang, A. Janotti, C. G. Van de Walle, and S. Stemmer, *Phys. Rev. B* **87**, 060101 (2013).
- ²⁰H. Rose, *Optik* **85**, 19 (1990).
- ²¹M. Haider, S. Uhlemann, E. Schwan, B. Kabius, and K. Urban, *Nature* **392**, 768 (1998).
- ²²C. L. Jia, L. Houben, A. Thust, and J. Barthel, *Ultramicroscopy* **110**, 500 (2010).
- ²³M. Lentzen, B. Jahn, C. L. Jia, A. Thust, K. Tillmann, and K. Urban, *Ultramicroscopy* **92**, 233 (2002).
- ²⁴C. Jia, S. Mi, M. Faley, U. Poppe, J. Schubert, and K. Urban, *Phys. Rev. B* **79**, 081405 (2009).
- ²⁵A. M. Glazer, *Acta Crystallogr., Sect. B* **28**, 3384 (1972).
- ²⁶J. Rodríguez-Carvajal, *Physica B* **192**, 55 (1993).
- ²⁷P. D. Nellist and S. J. Pennycook, "The principles and interpretation of annular dark-field z-contrast imaging," *Adv. Imaging Electron Phys.* **113**, 147–203 (2000).
- ²⁸P. D. Robb and A. J. Craven, *Ultramicroscopy* **109**, 61 (2008).
- ²⁹J. L. García-Muñoz, J. Rodríguez-Carvajal, P. Lacorre, and J. B. Torrance, *Phys. Rev. B* **46**, 4414 (1992).
- ³⁰See supplementary material at <http://dx.doi.org/10.1063/1.4881557> for figures and the HRTEM image calculation procedure.
- ³¹C. L. Jia, M. Lentzen, and K. Urban, *Science* **299**, 870 (2003).
- ³²K. Urban, C. L. Jia, L. Houben, M. Lentzen, S. B. Mi, and K. Tillmann, *Philos. Trans. R. Soc., A* **367**, 3735 (2009).
- ³³J. An, A. L. Koh, J. S. Park, R. Sinclair, T. M. Gür, and F. B. Prinz, *J. Phys. Chem. Lett.* **4**, 1156 (2013).
- ³⁴H. X. Yang, H. F. Tian, Z. Wang, Y. B. Qin, C. Ma, J. Q. Li, Z. Y. Cheng, R. Yu, and J. Zhu, *J. Phys.: Condens. Matter* **24**, 435901 (2012).
- ³⁵L. Lechner, J. Biskupek, and U. Kaiser, *Microsc. Microanal.* **18**, 379 (2012).